




Received June 21, 2019, accepted July 24, 2019, date of publication August 1, 2019, date of current version August 16, 2019.

Digital Object Identifier 10.1109/ACCESS.2019.2932431

Polymer-Based 3-D Printed Ku-Band Steerable Phased-Array Antenna Subsystem

SANG-HEE SHIN¹, (Student Member, IEEE), DIYAR F. ALYASIRI¹, MARIO D'AURIA¹,
WILLIAM J. OTTER¹ , CONNOR W. MYANT², DANIEL STOKES³,
ZHENGRONG TIAN³, NICK M. RIDLER³ , (Fellow, IEEE),
AND STEPAN LUCYSZYN¹ , (Fellow, IEEE)

¹Department of Electrical and Electronic Engineering, Imperial College London, London SW7 2AZ, U.K.

²Dyson School of Design Engineering, Imperial College London, London SW7 2AZ, U.K.

³Electromagnetic and Electrochemical Technologies Department, National Physical Laboratory, Teddington TW11 0LW, U.K.

Corresponding author: Stepan Lucyszyn (s.lucyszyn@imperial.ac.uk)

This work was supported in part by the UK Space Agency under Grant NSTP3-FT-046, and in part by the U.K. Engineering and Physical Sciences Research Council, under Grant EP/M001121/1 "TERACELL".

ABSTRACT This paper introduces the first fully 3-D printed tunable microwave subsystem, consisting of 26 circuit elements. Here, a polymer-based 3-D printed Ku-band 4-element steerable phased-array antenna with fully integrated beam-forming network is demonstrated. Polyjet was adopted for fabricating the main body of the subsystem, as it is capable of producing a geometrically complex structure with high resolution over a large volume. Low-cost fused deposition modeling was chosen to manufacture the dielectric inserts and brackets for the phase shifters. The measured radiation pattern revealed that the phased-array antenna subsystem has total beam steering angles of 54° and 52° at 15 GHz and 17 GHz, respectively. Excellent input return loss behavior was observed across the optimum operational frequency range of 15 to 17 GHz, with a worst-case measured return loss of 12.9 dB. This work clearly shows the potential of using 3-D printing technologies for manufacturing fully integrated subsystems with complex geometric features.

INDEX TERMS Additive manufacturing, 3-D printing, Polyjet, fused deposition modeling (FDM), ABS, PLA, Ku-band, rectangular waveguide, phased-array antenna.

I. INTRODUCTION

Phased array antennas are widely used for many applications, such as in modern radar and space communications systems. Phased-array antennas have many identical stationary antenna elements that form a steerable beam. It requires multiple sets of highly customized components, such as transmission lines or guided-wave structures, power splitters, phase shifters, feed networks and radiating elements [1]. Because these components are usually produced in small batches, perhaps requiring expensive bespoke manufacturing tools and lengthy turn-around times, the high fabrication cost is a major disadvantage when conventional subtractive manufacturing techniques are used (e.g., milling and machining).

Metal-pipe rectangular waveguides (MPRWGs) are widely used due to their low loss characteristics. However, as the structure gets smaller and more complicated, the manufacturing costs become a significant drawback. Over the past few years, various 3-D printing technologies have been studied

as alternative fabrication methods for rectangular waveguides and other associated radio frequency components [2]–[13]. Polymer-based 3-D printing technologies allow significant reductions in fabrication time, weight and cost, while ensuring near-comparable RF performance to their conventionally machined counterparts.

With conventional MPRWGs, components are manufactured as separate parts and assembled together to make a complete subsystem, requiring many waveguide flange connections; each contacting pair introducing a degradation in performance. In contrast, 3-D printing technologies allow more complex 3-D structures to be manufactured. Also, the number of parts can be significantly reduced with 3-D printing, minimizing the number of flanges.

The potential of using 3-D printing and surface metallization for microwave, millimeter-wave and terahertz applications have been demonstrated by several proof-of-principle devices. X- and W-band rectangular waveguides have been successfully developed with fused deposition modeling (FDM) and stereolithography (SLA) [2]. At Ku-band (12 to 18 GHz), different types of antennas,

The associate editor coordinating the review of this manuscript and approving it for publication was Hassan Tariq Chattha.

such as corrugated conical horn [4] and spline-profiled smooth horn antennas [5], were demonstrated using industrial FDM and SLA technologies, respectively. Using Poly-jet 3-D printing, a G-band waveguide, standard gain horn antenna and parabolic mirror have been manufactured giving measured performances close to their commercial counterparts [6]. 3-D printed MPRWGs has also been demonstrated at terahertz frequencies, requiring micrometer-level precision [7].

There is growing interest in utilizing the dielectric properties of polymer-based 3-D printed materials [8]. The dielectric properties of the polymers are easily tunable with composite filling materials and by varying infill densities. For example, using FDM 3-D printers, an X-band (8 to 12 GHz) termination has been manufactured and tested using a carbon filled polymer [14], while a broadband microwave gradient-index lens with varying infill density has also been demonstrated [15].

Polymer-based 3-D printing has been used to demonstrate relatively complex devices with repeating features, such as waveguide slot arrays [16], [17]. A linear 10-element dielectric-filled millimeter-wave horn antenna array was fabricated using SLA, in 2008, and showed an operational bandwidth from 35.0 to 39.5 GHz [18]. A more complicated antenna array, which includes components such as a flange, E-plane dividers and horn antennas, has been developed using SLA [19]. Similarly, a 2×2 antenna array with complicated waveguide feed network and conical horn antennas was developed to operate at Ka-band (26.5 to 40 GHz) [20].

Over the past two years, 3-D printed steerable antennas have been reported [21]–[23]. One was an S-band 6-element linear dipole array, made using multiple SLA-printed parts and needing six separate external feeds to provide steering [21]. Another was the electromagnetic simulation-only of a Ku-band frequency scanning slot array, having a scan angle of between -15.2° to $+15.4^\circ$ [22]. Finally, a resonant slot array has been demonstrated that employs mechanically moveable dielectric inserts to perform beam steering, employing SLA and FDM printing, respectively [23]. In that paper, the total beam steering angle is only 0 to 8.5° , using a conventionally manufactured metal screw-spring mechanism, over a 1% fraction bandwidth at 21.5 GHz, having a worst-case VSWR of 2.9.

This paper describes in detail the design, manufacture and measured results of a fully 3-D printed 4-element steerable phased-array antenna subsystem [24]. Here, 26 circuit elements ($1 \times$ flange, $6 \times$ mitred bends, $3 \times$ power splitters, $4 \times$ tunable delay lines, $4 \times 90^\circ$ waveguide twists, $4 \times$ bent interconnects and $4 \times$ H-plane sectoral horn antennas) are manufactured as a fully integrated, complete, subsystem. In addition, fully 3-D printed variable-position dielectric insertion mechanisms have been developed to implement tunable delay lines. All the measurements are performed by the UK's National Physical Laboratory, with reference to the UK's primary national measurement standards.

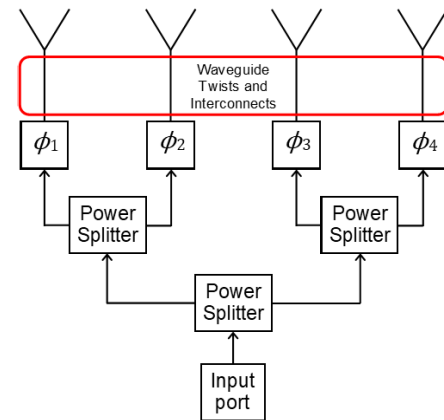


FIGURE 1. Basic block diagram of the 4-element phased-array antenna subsystem.

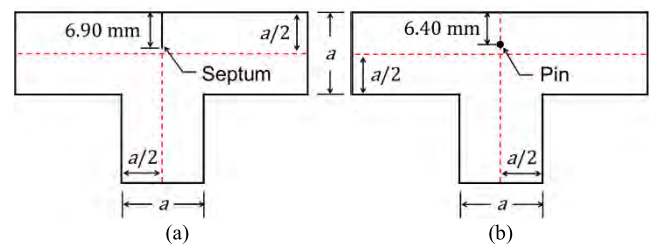


FIGURE 2. Illustration of 3 dB power splitter: (a) conventional design using a septum; and (b) pin solution.

II. DESIGN

The beamforming network and individual horn antennas have been designed as a fully-integrated phased-array subsystem. The basic block diagram of the beam-forming network and antenna array is shown in Fig. 1. The subsystem consists of 7 different types of MPRWG components: flange, bends, power splitters, tunable delay lines, twists, interconnects and horn antennas. All the waveguide components are based on conventional WR-62 waveguide, operating at Ku-band, having internal cross-sectional dimensions of $a = 15.799$ mm and $b = 7.899$ mm. The design has been optimized for operation between 15 and 17 GHz.

With the 4-element phased-array antenna, having a single input waveguide port, three symmetrical power splitters were introduced to create a 4-way corporate feed. Ideally, the conventional 3 dB power splitter design employs a thin metallic septum to achieve optimal performance. However, a 3-D printed thin vertical polymer wall is not structurally stable. Moreover, it may exhibit warping during the electroplating processes. Therefore, the septum was replaced by a 0.85 mm diameter cylindrical stainless-steel pin, with the use of electromagnetic software simulations to determine the optimal location. The two designs for the 3 dB power splitter are illustrated in Fig. 2.

A phase shifter is a control device found in many microwave communications, radar and measurement systems. There are subtle differences between the two main

generic types of phase shifter; true phase shifter and true delay line [25]. The former has a differential-phase group delay frequency response that does not change as the insertion phase is varied, within its defined bandwidth of operation. True phase shifters can be employed in multiple space diversity receiver combiners for aligning RF signals within a pulse envelope without changing the timing of the pulse edges. However, they should not be employed in wideband beam-forming networks for large aperture phased-array antennas, in order to avoid the effects of ‘phase squinting’ and ‘pulse stretching’. The latter has a differential-phase group delay frequency response that changes as the insertion phase is varied, within its defined bandwidth of operation. True delay lines find many applications in general wideband microwave signal processing applications, including beam-forming networks for phased-array antennas.

With phased-array antennas, phase steering and time steering are implemented by employing true phase shifters and true delay lines, respectively, as defined by the following:

True phase steering:

$$\Delta\phi = \Delta\phi(f) \text{ and } \theta(f) = \sin^{-1} \left\{ \frac{\lambda}{d} \cdot \frac{\Delta\phi}{360} \right\} \quad (1)$$

True time steering:

$$\Delta\phi(f) = \frac{f}{f_o} \Delta\phi(f_o) \text{ and } \theta = \sin^{-1} \left\{ \frac{\lambda}{d} \cdot \frac{\Delta\phi(f)}{360} \right\} \quad (2)$$

where, $\Delta\phi = \phi_i - \phi_{i-1}$ represent the difference in phase between the i^{th} and $i^{th} - 1$ antenna elements, θ is the steering angle from broadside boresight, f is the frequency, λ is the corresponding wavelength in free-space and subscript ‘o’ refers to the center frequency of the band of operation.

The authors recently published a 3-D printed MPRWG variable phase shifter that exploits a moveable dielectric flap insert, operating across X-band [13]. Its frequency behavior resembles a true phase shifter in the lower third of the band and a true delay line in the upper third of the band, with an undefined characteristic mid-band.

With the Ku-band design adopted in this work, the dielectric insert taper profile and insertion mechanism were completely redesigned to improve RF performance, structural stability and control. The dielectric insert was designed to be FDM 3-D printed using acrylonitrile butadiene styrene (ABS), with Formfutura’s Premium ABS (Frosty White), having X-band values of dielectric constant $\epsilon_r = 2.31$ and loss tangent $\tan\delta = 20 \times 10^{-4}$ [8]. The guided wavelength,

$$\lambda_g = \frac{\lambda}{\sqrt{\epsilon_{reff} - \left(\frac{\lambda}{2a}\right)^2}} \quad (3)$$

is dependent on the effective relative permittivity within the section of waveguide containing the dielectric insert ϵ_{reff} (with $1 < \epsilon_{reff} < \epsilon_r$). When the dielectric insert penetrates the region of maximum electric field for the dominant TE₁₀ mode, with more fractional volume filling the waveguide section, ϵ_{reff} increases and λ_g decreases [26]. As a result,

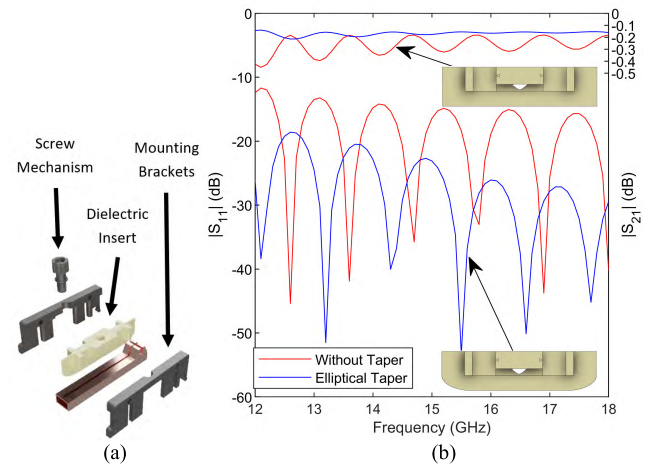


FIGURE 3. (a) Rendered CAD design of dielectric insert and brackets; (b) simulated insertion and return loss of phase shifter across Ku-band for 2 variations of dielectric insert shapes: Without and with elliptical taper.

transmission phase within the fixed length of delay line increases.

To achieve the maximum relative phase shift, and minimum losses, the dielectric inserts were designed to have a rectangular shape with elliptically tapered edges on both front and rear ends. 3-D printed brackets were designed to have a 3-D printed calibrated screw mechanism that inserts and extracts the dielectric pieces linearly and evenly through the slots. A pair of guide rails were added on each bracket to add extra stability. The computer-aided design (CAD) rendered drawing of a dielectric insert, bracket and screw mechanism are shown in Fig. 3(a).

Electromagnetic (EM) simulations were performed on the delay line section using ANSYS HFSS to optimize the size and shape of the tapered edges of the dielectric inserts. Simulated scattering (S-)parameter results are shown in Fig. 3(b), which clearly show that the elliptical taper shape has superior return and insertion loss behavior across Ku-band. With the dielectric insert at maximum depth, relative phase shifts of 262° and 288° are predicted at 15 and 17 GHz, respectively.

Figure 4 shows the predicted phase shifter performance for different levels of dielectric insert penetration depth g . The relative phase shift (when referenced to a non-penetrating dielectric insert) exhibits complicated features across the waveguide band; approximating to a true phase shifter at the lower band edge frequency, a true delay line at the upper band edge frequency and an undefined mid-band region. This is because a MPRWG is inherently a very frequency dispersive transmission medium. This resulting frequency behavior can also be seen in the X-band proof of principle [13]. The two phase shifting boundaries, seen in Fig. 4(a), are defined here by a 1° deviation from either true phase shifter or true delay line characteristics, for the reference level having $g = 0$. It can be seen, between 15 GHz and 17 GHz, the phase shifter resembles a true delay line for low levels of relative phase shift, but the undefined region extends further up in frequency with higher levels of relative phase shift.

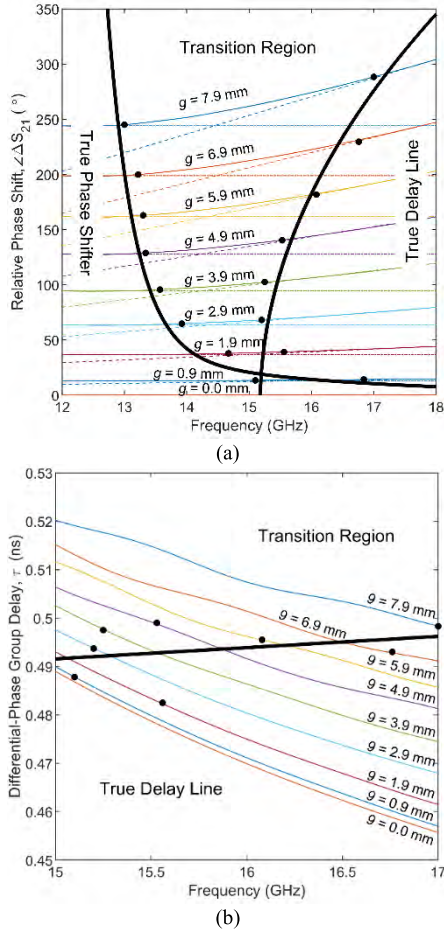


FIGURE 4. EM simulated phase shifter performance: (a) relative phase shift (when referenced to a non-penetrating dielectric insert having $g = 0$); and (b) differential-phase group delay response. Black dots represent the 1° deviation from either true phase shifter or true delay line characteristics (also mapped onto the differential-phase group delay characteristics) and the solid black lines represent the corresponding curve fits.

Figure 4(b) shows the corresponding differential-phase group delay frequency responses for the phase shifter between 15 GHz and 17 GHz. Clearly, the phase shifter exhibits true delay line characteristic in the region identified in Fig. 4(b), with this approximation being poorer in the transition region.

The independent tunable phase shifters are followed by 90° twists, followed by bent waveguide interconnects required to feed the individual H-plane sectoral horn antennas, while maintaining equal delay paths when there is no steering from the broadside boresight. For optimal performance, the distance between each array element d is set to half the free-space wavelength $\lambda = 20$ mm at 15 GHz (i.e., $d = \lambda(15 \text{ GHz})/2 = 10$ mm). A WR-62 based H-plane sectoral horn antenna is ideal for achieving this, as its E-plane height dimension is sufficiently smaller than the operational free-space wavelength (i.e., $b < \lambda(15 \text{ GHz})/2$). The internal dimensions for the H-plane sectoral horn antenna design are shown in Fig. 5.

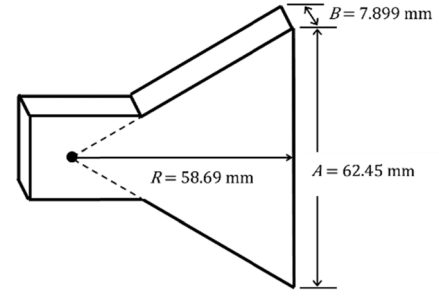


FIGURE 5. Illustration of the H-plane sectoral horn design.

With infinitesimally thin metal walls made with a perfect electrical conductor (PEC), the theoretical directivity of the single horn antenna D_e is [27], [28],

$$D_e(\text{dB}) = 10 \cdot \log_{10} \left\{ \varepsilon_t \varepsilon_{ph}^H \cdot \frac{4\pi}{\lambda^2} \cdot Ab \right\} = \begin{cases} 9.8 & \text{at 15 GHz} \\ 10.5 & \text{at 17 GHz} \end{cases} \quad (4)$$

where, the aperture taper efficiency factor $\varepsilon_t = 8/\pi^2$ and the phase efficiency factor is given by [27]:

$$\varepsilon_{ph}^H = \frac{\pi^2}{64\xi} \cdot \left\{ [C(p_1) - C(p_2)]^2 + [S(p_1) - S(p_2)]^2 \right\} \quad (5)$$

and parameters p_1 and p_2 are [28],

$$p_1, p_2 = \frac{1}{\sqrt{2}} \cdot \left[(8\xi)^{-\frac{1}{2}} \pm (8\xi)^{\frac{1}{2}} \right] \quad (6)$$

and the Fresnel integrals, $S(x)$ and $C(x)$ are a function of the fractional aperture distribution phase error ξ ,

$$\xi = \frac{A^2}{8\lambda R} = \begin{cases} 0.42 & \text{at 15 GHz} \\ 0.47 & \text{at 17 GHz} \end{cases} \quad (7)$$

The complete phased-array antenna's broadside boresight directivity (D_A) was calculated using [27]:

$$D_A(\text{dB}) = D_e(\text{dB}) + D_i(\text{dB}) = \begin{cases} 15.8 & \text{at 15 GHz} \\ 17.1 & \text{at 17 GHz} \end{cases} \quad (8)$$

where, the directivity for a broadside linear array of N uniformly-excited isotopically radiating elements is,

$$D_i(\text{dB}) = 10 \cdot \log_{10} \left\{ 2N \frac{d}{\lambda_0} \right\} = \begin{cases} 6.0 & \text{at 15 GHz} \\ 6.6 & \text{at 17 GHz} \end{cases} \quad (9)$$

Our electromagnetic CAD simulations assume PEC metalization (which represents a good approximation to copper at Ku-band), but with metal wall thicknesses for the horns corresponding to those in the actual prototype antenna array. This dramatically reduces radiation backlobe levels (by reducing the backward radiation leakage caused by knife-edge diffraction that results from infinitesimal thin walls) and, thus, increases predicted antenna gain at boresight beyond that calculated in (8).

CAD drawings for the main body of the phased-array antenna are shown in Fig. 6. To validate the final design of

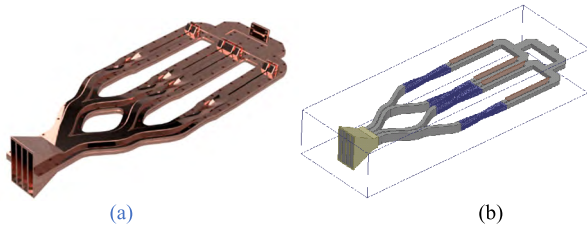


FIGURE 6. CAD design of the main body of the phased-array antenna subsystem: (a) rendered 3-D model; and (b) simulation model with radiation boundary.

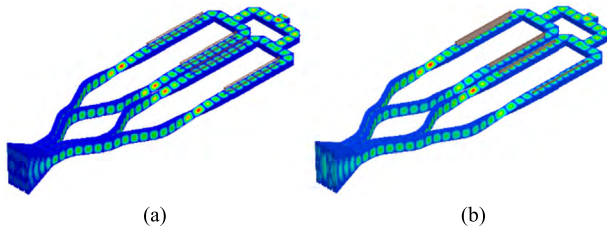


FIGURE 7. Simulated internal E-field patterns at 15 GHz: (a) with all the dielectric inserts fully inserted; and (b) with dielectric insertion setting for maximum beam steering angle.

the complete phased-array antenna subsystem, simulations were performed using HFSS with PEC waveguide walls (to minimize the computational resources needed for such a large and complicated structure). Fig. 7 shows the simulated internal E-field patterns at 15 GHz, with all the individual components functioning as expected. For example, it can be seen in Fig. 7(b), when a dielectric insert has maximum penetration it accommodates an extra $\sim 3\lambda_g/4$, when compared to zero penetration.

III. MANUFACTURE

To manufacture the complete phased-array antenna subsystem, two types of 3-D printing technologies were employed: (i) Polyjet, an industrial-level process with ultra-high precision; and (ii) low-cost, entry-level desktop FDM.

A. POLYJET 3D PRINTING

A Polyjet 3-D printer (Stratasys Objet500 Connex3) was used for fabricating the MPRWG parts of the phased-array antenna subsystem. This printer is capable of printing large models at high resolution (maximum build area of $490 \text{ mm} \times 390 \text{ mm} \times 200 \text{ mm}$, with a minimum layer height of $16 \mu\text{m}$) by using its polymer jetting technology. The Polyjet printer jets photopolymer droplets that solidify when cured by an internal ultraviolet (UV) light source. It utilizes wax-like support material that allows the 3-D printer to print complex geometric features, such as curves and twists at the required resolution.

The main body of the phased-array antenna subsystem was printed in only two pieces; the top and bottom half parts were printed separately for ease of cleaning and metallization. A Polyjet resin, VeroWhite, was used for the main body. VeroWhite provides rigid 3D prints that offers high resolution comparable to injection-molded polymer counterparts. The

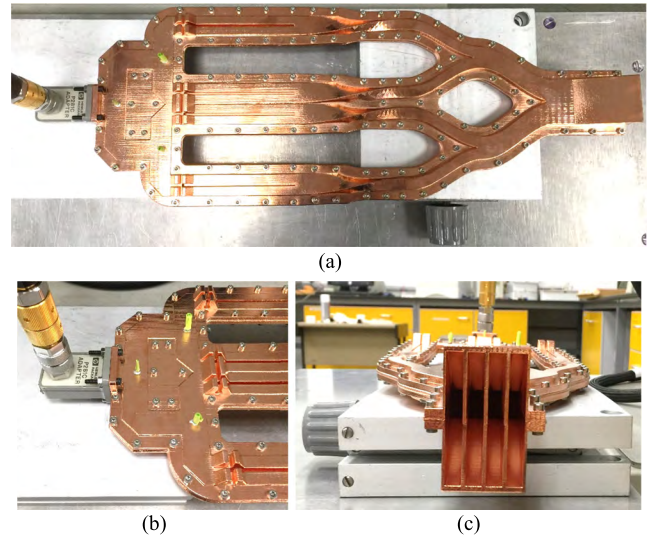


FIGURE 8. Assembled phased-array antenna without dielectric insert components: (a) top view; (b) close-up view showing the waveguide port, power splitter pins, and phase shifter slot; and (c) close-up view showing aperture of horn antennas.

support material was mechanically removed and cleaned with a high-pressure water jet.

B. FDM 3D PRINTING

Fused deposition modeling 3-D printing was used to manufacture the dielectric inserts for the tunable phase shifters, their mounting brackets and calibrated screw mechanisms. The dielectric inserts were fabricated using an Ultimaker 2 printer, with Formfutura's Premium ABS (White) filament. Using a slicing software, Ultimaker Cura [29], the prints were set for a $100 \mu\text{m}$ layer height. The 3-D models of the inserts were orientated perpendicular to the build surface of the printer, in order to minimize the need for support structures. Infill parameters were customized to give a theoretical 100% infill density. The brackets and screw mechanisms were fabricated using an Original Prusa i3 MK3, with polylactic acid (PLA) filaments. The FDM parts were all lightly sanded-down to increase their smoothness for ease in assembly and operation. Moreover, to reduce friction, petroleum jelly was applied to the screws.

C. METAL ELECTROPLATING PLATING

After cleaning, to metalize the main body of the phased-array antenna, a commercial copper-electroplating metallization process was employed. The electroplating process gave a copper layer thickness of $20 \mu\text{m}$, corresponding to 38 skin depths (with $\delta = 0.53 \mu\text{m}$ at 15 GHz). The skin depth is given by $\delta = \sqrt{\rho_o / (\pi f_{min} \mu_o)}$, where the resistivity of copper $\rho_o = 1.72 \times 10^{-8} \Omega \cdot \text{m}$, f_{min} is the minimum operating frequency and μ_o is the permeability of free-space. The electroplated parts were assembled with standard M3 screws and nuts, as shown in Fig. 8. Note that these M3 screws can be 3-D printed, or replaced altogether using conductive adhesive, in order to achieve further weight savings.

TABLE 1. Predicted main body mass comparison (without nuts and bolts) for 3-D printed and conventionally machined phased-array antenna.

Manufacturing Method	Total Mass (g)	Conventional / 3-D Printed Mass Ratio
Conventional Aluminum	1026*	2.0
Conventional Copper	3397*	6.5
3-D Printed & Electroplated	522	-

* Predicted values from CAD software (Autodesk Fusion 360).

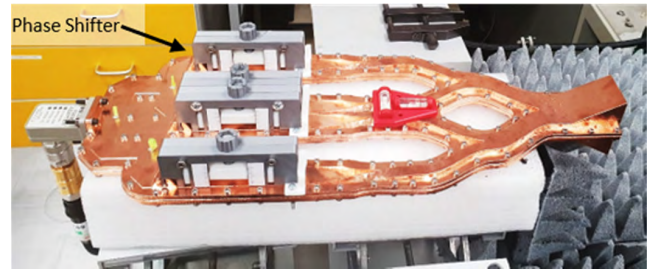
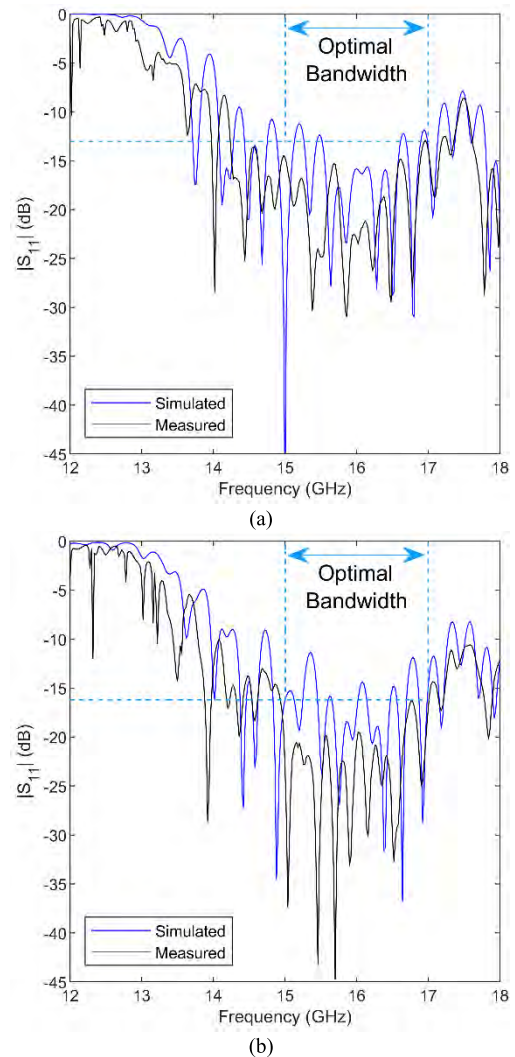
As weight reduction is one of the most appealing aspects of using polymer-based 3-D printing, the mass of the main body parts of the phased-array antenna was measured after the electroplating process. Predicted masses of conventionally machined solid-copper and aluminium phased-array antennas were obtained using CAD software (Autodesk Fusion 360) for comparison. The results are given in Table 1. As expected, polymer-based 3-D printing offers significant mass reduction when compared to conventional machining. Compared with conventional (i.e., non-3-D printing) commercial waveguide implementation, the mass reduction will be even greater, as multiple flanges are required to connect individual components together.

IV. MEASUREMENTS

Three sets of measurements were made at NPL: (i) input return loss; (ii) phase shift; and (iii) radiation pattern. The first two were taken using a vector network analyzer (Agilent PNA). Calibration standards with traceability to the International System of units (SI), via their mechanical dimensions, were used to provide accurate S-parameter measurements with reference planes at the waveguide test ports. This was achieved by performing a Thru-Reflect-Line (TRL) calibration [30]. This calibration employed Ku-band waveguide standards: Thru – connecting the two VNA test ports together; Reflect – using a flush short-circuit connected, in turn, to each VNA test port; Line – using a $\frac{1}{4}$ -wave section of waveguide. The length of the $\frac{1}{4}$ -wave line was 6.4 mm, which is the optimum length for calibration (i.e., by providing a phase shift of a $\frac{1}{4}$ of a guided wavelength) in the middle of the waveguide band (i.e., *ca.* 15 GHz for Ku-band waveguide).

The calibration was performed using an in-house calibration algorithm, employing a seven-term error-correction routine [31]. The complete measurement set-up (i.e., VNA, primary reference standards and calibration algorithm) is referred to as the NPL primary impedance microwave measurement system (PIMMS) [32], [33] and represents the UK's primary national standard system for S-parameter measurements.

The radiation patterns were measured in one of NPL's anechoic chambers, which comprises a transmit tower with reference antenna, a phi-over-theta spherical positioner system for the receiving antenna under test and associated RF test equipment operating from 0.5 to 220 GHz [34].

**FIGURE 9. Return loss measurement set-up with dielectric inserts (fully assembled).****FIGURE 10. Simulated and measured return loss of phased-array antenna across Ku-band: (a) without dielectric inserts; and (b) maximum dielectric insertion.**

To accurately determine the gain of the antenna under test, it is critical to calibrate the gain of the reference antenna (standard gain horn) with a low uncertainty. Prior to the radiation pattern measurement for the phased-array, the gain of the reference antenna (Narda 639B, having measured gains of 16.39 and 17.32 dBi at 15 and 17 GHz, respectively) was calibrated using the three-antenna extrapolation technique [35] with an uncertainty of 0.05 dB.

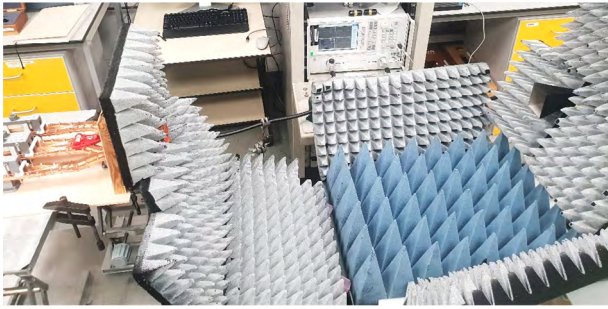


FIGURE 11. Relative phase shift measurement set-up.

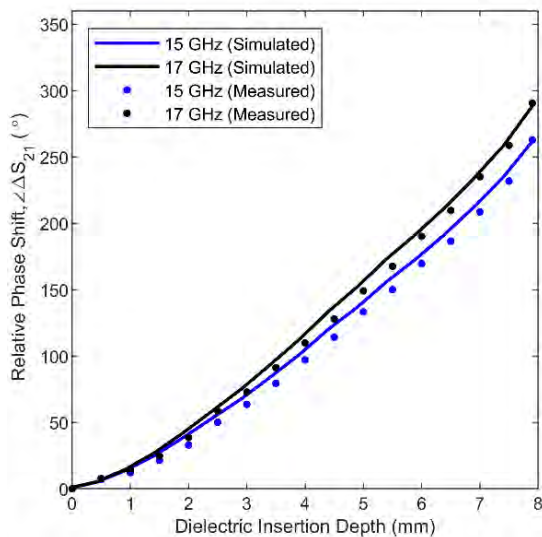


FIGURE 12. Simulated and measured relative phase shift at 15 and 17 GHz.

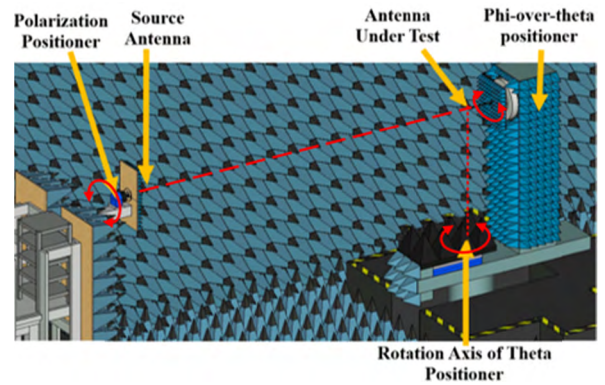
A. RETURN LOSS MEASUREMENT

The input return loss for the complete phased-array antenna subsystem was measured as a function of dielectric insert penetration depth, across Ku-band, using the measurement set-up shown in Fig. 9. Radar absorbing material (RAM) was placed in surrounding areas to minimize reflections. The measurement uncertainty for return loss was expected to be ± 0.2 dB at 20 dB.

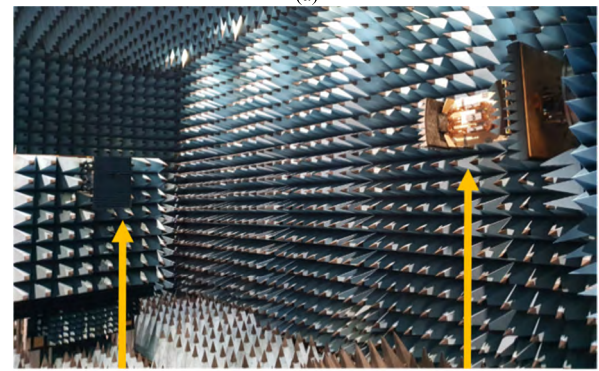
The EM simulated and measured return loss results across Ku-band are shown in Fig. 10. The phased-array antenna shows excellent return loss behavior between 15 and 17 GHz. It can be seen that the measured return loss without any dielectric inserts is better than 12.9 dB across the 15 and 17 GHz operating frequency range. When the dielectric inserts are at maximum depth, the worst-case return loss is 16.3 dB.

B. PHASE SHIFTER MEASUREMENTS

The relative phase shift of the phased-array antenna is the same as that for the individual phase shifters, when they are all in phase with one another. This was measured at 15 and 17 GHz, using the measurement set-up shown in Fig. 11. The phased-array antenna and a receiving horn antenna



(a)



(b)

FIGURE 13. NPL's anechoic chamber far-field antenna measurement set-up: (a) Standard measurement illustration; and (b) Photograph showing the phased-array antenna during H-plane measurements.

were attached to fixed mounts with the boresight of the array aligned with the receiver horn. The separation distance between the two antenna apertures was 0.96 m (below the combined radiating far-field distance of 1.82 m). The measurement uncertainty for transmission phase was expected to be 0.6° .

Using the screw mechanism, all four dielectric inserts were set to give the same level of penetration for each measurement. Starting from maximum insertion, measurements took place for every 0.5 mm of extraction. A Vernier caliper with resolution of 0.01 mm was used as a calibration reference. There was no significant drift observed between each measurement.

The simulated and measured relative phase shift performance at 15 and 17 GHz is shown in Fig. 12. Despite spatial uncertainty associated with measuring penetration depth and their relative alignments, the simulated and measured results show excellent agreement. From measured insertion phase $\angle S_{21}$, a maximum relative phase shift $\Delta \angle S_{21}(15 \text{ GHz}) = 263^\circ$ and $\Delta \angle S_{21}(17 \text{ GHz}) = 290^\circ$, which are within 0.4% and 0.7% of their respective predicted values.

C. RADIATION PATTERN MEASUREMENTS

The far-field E- and H-plane radiation patterns were measured at NPL's spherical test range. The spherical test range

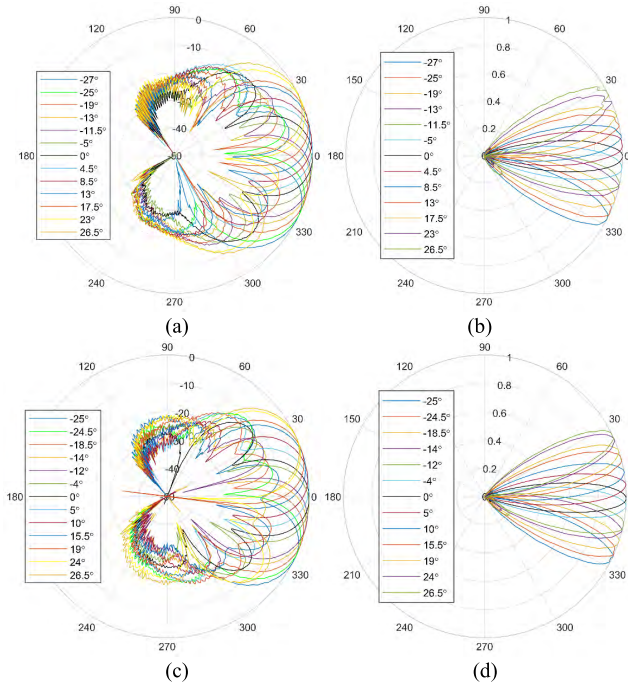


FIGURE 14. Measured far-field E-plane radiation patterns at 15 and 17 GHz, normalized to the broadside boresight value: (a) 15 GHz (logarithmic); (b) 15 GHz (linear); (c) 17 GHz (logarithmic); and (d) 17 GHz (linear).

is housed within a temperature-controlled ($23 \pm 1^\circ\text{C}$), $15 \times 7.5 \times 7.5 \text{ m}^3$, fully-screened anechoic chamber.

The phased-array antenna subsystem was mounted on a phi-over-theta spherical positioner, illustrated in Fig. 13, with its aperture aligned over the rotation axis of the theta positioner. A WR-62 standard gain horn was used as the source antenna, which was installed on the polarization positioner. The separation distance between the source antenna and the phased-array antenna was 6 m.

The combined radiating far-field (Fraunhofer) distance $R(17 \text{ GHz}) = 2(D_{STD}^2 + D_{PAA}^2)/\lambda = 1.3 \text{ m}$, where $D_{STD} = 71 \text{ mm}$ and $D_{PAA} = 80 \text{ mm}$ are the maximum aperture size for the standard gain horn and phased-array antennas, respectively. The gain of the phased-array antenna was determined using a transfer method [36], by comparing with that of the commercial standard gain horn antenna. The uncertainty for the antenna gain measurement was expected to be approximately $\pm 1 \text{ dB}$.

The penetration depths of the dielectric inserts were pre-calibrated to scan between the simulated target minimum and maximum beam steering angles $\theta_{max,min}$, in 5° increments. The phase difference between antenna elements $\Delta\phi(f)_{max}$, to achieve the maximum and minimum beam steering angles, was calculated using:

$$\Delta\phi(f)_{max} = \frac{\Delta\angle S_{21}(f)_{max}}{3} = \begin{cases} \pm 87^\circ & \text{at 15 GHz} \\ \pm 96^\circ & \text{at 17 GHz} \end{cases} \quad (10)$$

where, $\Delta\angle S_{21max}$ is the simulated relative phase shift, at maximum dielectric penetration $g = 7.9 \text{ mm}$. The intermediate

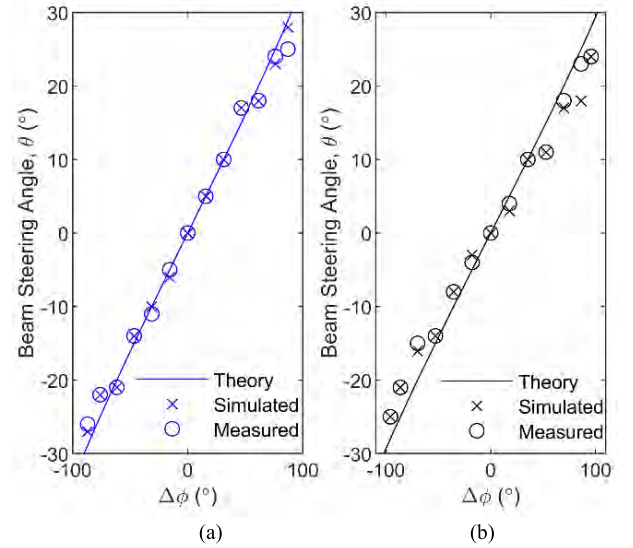


FIGURE 15. Theoretical, EM simulated and measured beam steering angles: (a) 15 GHz; and (b) 17 GHz.

values of $\Delta\phi(f)$ for achieving the target beam steering angle θ were calculated using the true time steering expression in (2),

$$\Delta\phi(f) = \frac{d}{\lambda} \cdot \sin\{\theta\} \cdot 360^\circ \quad (11)$$

Using $\Delta\phi(f)$, the relative phase for the i^{th} phase shifter element was obtained from $\phi_i(f) = (i - 1) \cdot \Delta\phi(f)$, where $i \in \{1, 2, 3, 4\}$. The dielectric insert penetration depth corresponding to each value of $\phi_i(f)$ was interpolated from simulated relative phase shift given in Fig. 12. From Fig. 4(a), it can be seen that the phase shifter approximates to a true time shifter at 17 GHz, while having a transition characteristic at 15 GHz. The calibrated dielectric insert penetration depth settings are shown in Table 2.

To ensure the dielectric inserts are in the right positions, small 3-D printed calibration blocks were placed at the bottom of the rails, on the phase shifter brackets, which prevent the dielectric inserts from penetrating further than the calibrated values during the measurements.

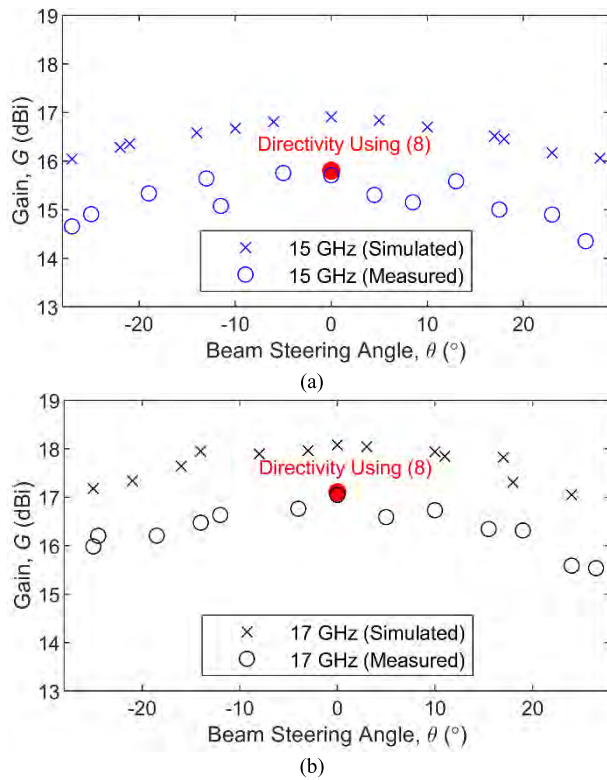
Measured far-field E-plane radiation patterns are shown in Fig. 14. It can be seen that the total beam steering angle is 54° at 15 GHz and 52° at 17 GHz. By controlling the dielectric insert penetration depth, the phased-array antenna's beam angle can be adjusted to scan between -27° and $+27^\circ$ at 15 GHz and -25° and $+27^\circ$ at 17 GHz.

Figure 15 shows predicted (theoretical and EM simulated) and measured beam steering angles from broadside boresight for each phase shift setting. The theoretical results can be obtained directly using either (1) or (2). For both 15 and 17 GHz, measured results show excellent agreement with the predicted results.

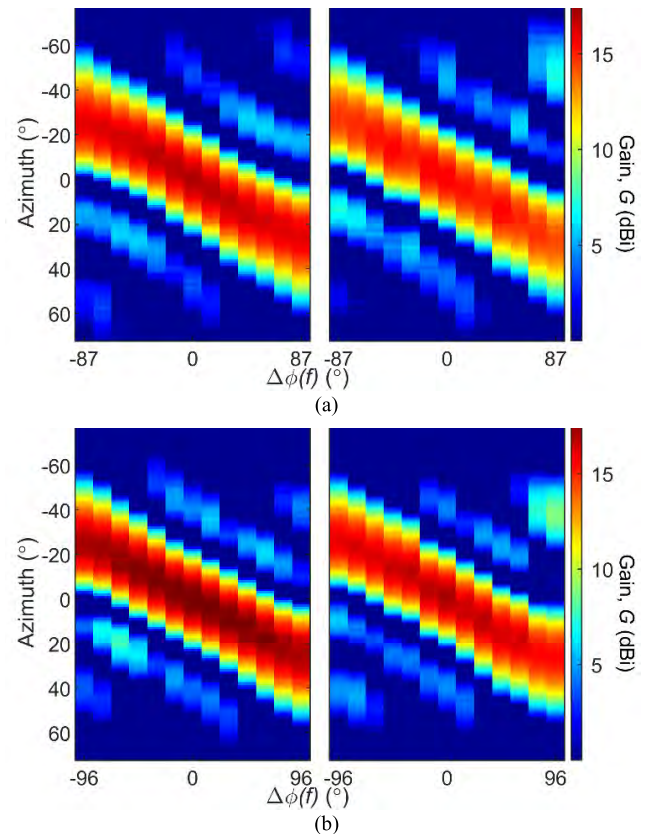
The antenna gains for each target beam steering angle ranges from 14.4 to 15.8 dBi at 15 GHz and from 15.5 to 17.0 dBi at 17 GHz. At broadside boresight, the theoretical prediction and measured results show

TABLE 2. Calibrated dielectric insert penetration depth settings.

Target Beam Steering Angle, θ ($^{\circ}$)	Phase Difference Between Antenna Elements, $\Delta\phi(f)$ ($^{\circ}$)		Required Relative Phase Shift $\Delta\angle S_{21}$ ($^{\circ}$) for Individual Phase Shifters								Dielectric Insert Penetration Depth, g (mm)			
			$\phi_1(f)$		$\phi_2(f)$		$\phi_3(f)$		$\phi_4(f)$		g_1	g_2	g_3	g_4
	15 (GHz)	17 (GHz)	15 (GHz)	17 (GHz)	15 (GHz)	17 (GHz)	15 (GHz)	17 (GHz)	15 (GHz)	17 (GHz)				
Minimum	-87	-96	262	288	175	192	87	96	0	0	7.9	5.9	3.5	0
-25	-76	-86	228	259	152	173	76	86	0	0	7.3	5.3	3.2	0
-20	-62	-70	185	209	123	140	62	70	0	0	6.2	4.5	2.7	0
-15	-47	-53	140	159	93	106	47	53	0	0	5.0	3.7	2.2	0
-10	-31	-35	94	106	63	70	31	35	0	0	3.7	2.7	1.7	0
-5	-16	-18	47	53	31	36	16	18	0	0	2.2	1.7	1	0
0	0	0	0	0	0	0	0	0	0	0	0	0	0	0
5	16	18	0	0	16	18	31	36	47	53	0	1.0	1.7	2.2
10	31	35	0	0	31	35	63	70	94	106	0	1.7	2.7	3.7
15	47	53	0	0	47	53	93	106	140	159	0	2.2	3.7	5.0
20	62	70	0	0	62	70	123	140	185	209	0	2.7	4.5	6.2
25	76	86	0	0	76	86	152	173	228	259	0	3.2	5.3	7.3
Maximum	87	96	0	0	87	96	175	192	262	288	0	3.5	5.9	7.9

**FIGURE 16.** EM simulated and measured antenna gains at 15 and 17 GHz against beam steering angle: (a) 15 GHz; and (b) 17 GHz.

exceptional agreement; the measured gains of $G(15 \text{ GHz}) = 15.7 \text{ dBi}$ and $G(17 \text{ GHz}) = 17.0 \text{ dBi}$ are both only 0.1 dB lower than the calculated directivities. This is because, in practice, approximately the same amount of energy lost through backward radiation leakage (as a result of knife-edge diffraction and inferred by the theoretical predictions using (8)) is also lost through the dominant transmission losses in the practical demonstrator prototype. The EM simulated (with PEC metallization and no surface roughness or defects) and measured gains for the phased-array antenna are shown in Fig. 16. There are approximately 1.5 dB

**FIGURE 17.** EM simulated (left) and measured (right) radiated E-plane field intensities: (a) 15 GHz; and (b) 17 GHz.

and 1 dB differences at 15 GHz and 17 GHz, respectively. These discrepancies can be attributed to the finite conductivity of the metallization, surface roughness and small defects [37].

For each target value of $\Delta\phi(f)$, given in Table 2, the EM simulated and measured E-plane field intensity are shown in Fig. 17. The E-field intensity peak represents the location and size of the main lobe and any sidelobes. It can be seen that for both 15 GHz and 17 GHz, simulated and measured

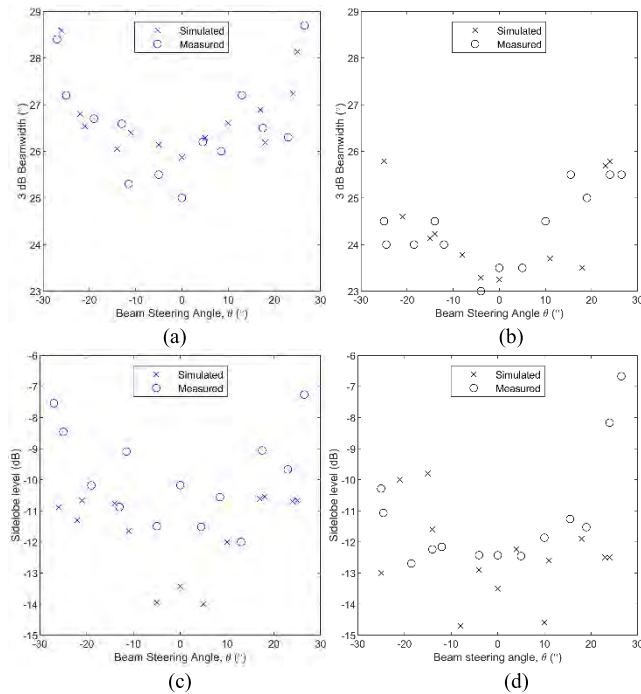


FIGURE 18. EM simulated and measured E-plane radiation pattern properties: (a) 3 dB beamwidths at 15 GHz; (b) 3 dB beamwidths at 17 GHz; (c) worst-case sidelobe levels at 15 GHz; and (d) worst-case sidelobe levels at 17 GHz.

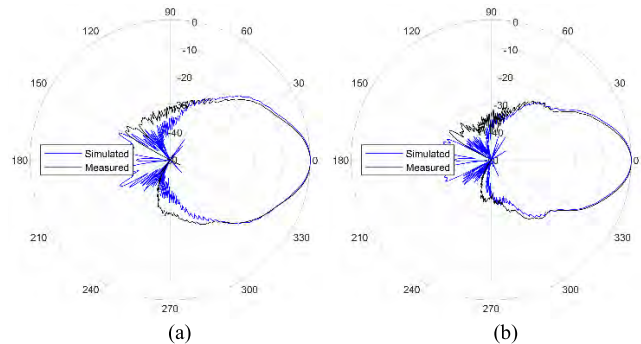


FIGURE 19. EM simulated and measured far-field H-plane radiation patterns: (a) 15 GHz (logarithmic); and (b) 17 GHz (logarithmic).

results have similar beam profiles, with approximately the same sizes and locations of the main lobe and sidelobes.

The EM simulated and measured E-plane radiation pattern properties are shown in Fig. 18. The 3 dB beamwidths for each beam steering angle are shown on Fig. 18(a) and 18(b). The phased-array antenna shows almost identical performance to predictions at 15 GHz and 17 GHz. The maximum measured beamwidths are 29° and 26° at 15 GHz and 17 GHz, respectively. The minimum measured beamwidths are 25° and 23° at 15 GHz and 17 GHz, respectively.

The worst-case sidelobe levels for each beam steering angle are shown on Fig. 18(c) and 18(d). There is close agreement between the simulated and measured sidelobe levels. At 15 GHz, more than half of the measured sidelobe levels are below −10 dB, but higher than the simulated results. At 17 GHz, the results improve with most of the measured

sidelobe levels below −10 dB. The worst-case measured sidelobe levels are −7.3 dB and −6.7 dB at 15 GHz and 17 GHz, respectively. The 3 dB beamwidth and sidelobe levels can be reduced by further optimizing the dielectric penetration depth and improving control accuracy of the dielectric insertion mechanism.

Finally, far-field H-plane radiation patterns were measured at broadside boresight without the dielectric inserts. The EM simulated and measured results are shown in Fig. 19. The measured 3 dB beamwidths are 24° and 22° at 15 GHz and 17 GHz, respectively, which are nearly identical to the simulated results. It is interesting to note that the 3 dB beamwidths for the complete phased-array antenna, at broadside boresight, for the H-plane are approximately only 1° less than those for the E-plane.

These results show that even with finite conductivity walls, rough surfaces and defects, the manufactured 3-D printed phased-array's performance is comparable to that of an ideal model having PEC metallization and no surface roughness or defects.

V. DISCUSSION AND CONCLUSION

This paper has introduced the first fully 3-D printed tunable microwave subsystem. The Ku-band 4-element phased-array antenna was manufactured using polymer-based 3-D printing technologies, consisting of 26 circuit elements, and demonstrated excellent measured performance. A combination of industrial-level Polyjet technology and entry-level FDM was used to print the phased-array antenna. By independently adjusting the depths of the dielectric inserts, the beam was fully steerable from −27° to +27° at 15 GHz and −25° to +27° at 17 GHz. Measured beam profiles and antenna gains show excellent agreement with simulated results.

This work shows that 3-D printing technologies are capable of producing low-cost and high-performance devices, not only at component level but also at subsystem levels. It is evident that with further research, this technology will be able to replace more conventional manufacturing and design method for RF applications. Possible areas of future research include: (i) wider bandwidth designs; (ii) integrating other tunable components, such as variable attenuators, power splitters and filters; (iii) providing multifunctionality to reduce overall size and mass; (iv) comparing metallization processes (electroplating, drip coating, spray painting, vacuum metallization, etc.); and (v) material characterization for dielectric inserts.

ACKNOWLEDGMENT

This paper is an expanded version from the IEEE MTT-S International Microwave Workshop Series on Advanced Materials and Processes 2019, Bochum, Germany, July, 2019. The authors would like to thank Dr. X. Shang and J. Skinner at NPL for arranging the electroplating and R. Payapulli at ICL.

REFERENCES

- [1] R. J. Mailloux, "Phased Arrays in Radar and Communication System," in *Phased Array Antenna Handbook*, 2nd ed. Boston, MA, USA: Artech House, 2005, pp. 1–59.

- [2] M. D'Auria, W. J. Otter, J. Hazell, B. T. W. Gillatt, C. Long-Collins, N. M. Ridler, and S. Lucyszyn, "3-D printed metal-pipe rectangular waveguides," *IEEE Trans. Compon., Packag., Manuf. Technol.*, vol. 5, no. 9, pp. 1339–1349, Sep. 2015.
- [3] W. J. Otter and S. Lucyszyn, "Printing: The future of THz," *IET Electron. Lett.*, vol. 53, no. 7, p. 433, Mar. 2017.
- [4] J. C. S. Chieh, B. Dick, S. Loui, and J. D. Rockway, "Development of a Ku-band corrugated conical horn using 3-D print technology," *IEEE Antennas Wireless Propag. Lett.*, vol. 13, pp. 201–204, Feb. 2014.
- [5] M. van der Vorst and J. Gumpinger, "Applicability of 3D printing techniques for compact Ku-band medium/high-gain antennas," in *Proc. 10th Eur. Conf. Antennas Propag. (EuCAP)*, Davos, Switzerland, Apr. 2016, pp. 1–4.
- [6] S. Lucyszyn, X. Shang, W. J. Otter, C. W. Myant, R. Cheng, and N. M. Ridler, "Polymer-based 3D printed millimeter-wave components for spacecraft payloads," in *Proc. IEEE MTT-S Int. Microw. Workshop Series Adv. Mater. Process. (IMWS-AMP)*, Ann Arbor, MI, USA, Jul. 2018, pp. 1–3.
- [7] W. J. Otter, N. M. Ridler, H. Yasukochi, K. Soeda, K. Konishi, J. Yumoto, M. Kuwata-Gonokami, and S. Lucyszyn, "3D printed 1.1 THz waveguides," *Electron. Lett.*, vol. 53, no. 7, pp. 471–473, Mar. 2017.
- [8] J. Sun, A. Dawood, W. J. Otter, N. M. Ridler, and S. Lucyszyn, "Microwave characterization of low-loss FDM 3-D printed ABS with dielectric-filled metal-pipe rectangular waveguide spectroscopy," *IEEE Access*, vol. 7, pp. 95455–95486, 2019.
- [9] B. Zhang and H. Zirath, "3D printed iris bandpass filters for millimetre-wave applications," *Electron. Lett.*, vol. 51, no. 22, pp. 1791–1793, Oct. 2015.
- [10] B. Al-Juboori, J. Zhou, Y. Huang, M. Hussein, A. A. Ieldin, W. J. Otter, D. Klugmann, and S. Lucyszyn, "Lightweight and low-loss 3-D printed millimeter-wave bandpass filter based on gap-waveguide," *IEEE Access*, vol. 7, no. 1, pp. 2624–2632, Jan. 2019.
- [11] W. J. Otter and S. Lucyszyn, "Hybrid 3-D-printing technology for tunable THz applications," *Proc. IEEE*, vol. 105, no. 4, pp. 756–767, Apr. 2017.
- [12] A. Genc, T. Goksu, and S. Helhel, "Fabrication of three-dimensional printed rectangular waveguide T-junction with in-phase and equal power division," *Microw. Opt. Technol. Lett.*, vol. 60, no. 8, pp. 2043–2048, 2018.
- [13] B. T. W. Gillatt, M. D'Auria, W. J. Otter, N. M. Ridler, and S. Lucyszyn, "3-D printed variable phase shifter," *IEEE Microw. Wireless Compon. Lett.*, vol. 26, no. 10, pp. 822–824, Oct. 2016.
- [14] Y. Arbaoui, V. Laur, A. Maalouf, P. Quéffélec, D. Passerieux, A. Delias, and P. Blondy, "Full 3-D printed microwave termination: A simple and low-cost solution," *IEEE Trans. Microw. Theory Techn.*, vol. 64, no. 1, pp. 271–278, Jan. 2016.
- [15] S. Zhang, Y. Vardaxoglou, W. Whittow, and R. Mittra, "3D-printed flat lens for microwave applications," in *Proc. Loughborough Antennas Propag. Conf. (LAPC)*, Loughborough, U.K., Nov. 2015, pp. 1–3.
- [16] G. P. Le Sage, "3D printed waveguide slot array antennas," *IEEE Access*, vol. 4, pp. 1258–1265, Mar. 2016.
- [17] G. McKerricher, A. Nafe, and A. Shamim, "Lightweight 3D printed microwave waveguides and waveguide slot antenna," in *Proc. IEEE Int. Symp. Antennas Propag. USNC/URSI Nat. Radio Sci. Meeting*, Vancouver, BC, Canada, Jul. 2015, pp. 1322–1323.
- [18] L. Schulwitz and A. Mortazawi, "A compact millimeter-wave horn antenna array fabricated through layer-by-layer stereolithography," in *Proc. IEEE Antennas Propag. Soc. Int. Symp.*, San Diego, CA, USA, Jul. 2008, pp. 1–4.
- [19] B. Rohrdantz, C. Rave, and A. F. Jacob, "3D-printed low-cost, low-loss microwave components up to 40 GHz," in *Proc. IEEE MTT-S Int. Microw. Symp. (IMS)*, San Francisco, CA, USA, May 2016, pp. 1–3.
- [20] A. I. Dimitriadis, T. Debogovic, M. Favre, M. Billod, L. Barloggio, J. Ansermet, and E. D. Rijk, "Polymer-based additive manufacturing of high-performance waveguide and antenna components," *Proc. IEEE*, vol. 105, no. 4, pp. 668–676, Apr. 2017.
- [21] M. Mirmozafari, S. Saedi, H. Saedi-Manesh, G. Zhang, and H. H. Sigmarsson, "Direct 3-D printing of nonplanar linear-dipole-phased array antennas," *IEEE Antennas Wireless Propag. Lett.*, vol. 17, no. 11, pp. 2137–2140, Nov. 2018.
- [22] K. Zhao, G. Senger, and N. Ghalichechian, "3D-printed frequency scanning slotted waveguide array with wide band power divider," in *Proc. United States Nat. Committee URSI Nat. Radio Sci. Meeting (USNC-URSI NRS)*, Boulder, CO, USA, Jan. 2019, pp. 1–2.
- [23] G. P. Le Sage, "Dielectric steering of a 3-D printed microwave slot array," *IEEE Antennas Wireless Propag. Lett.*, vol. 17, no. 11, pp. 2141–2144, Nov. 2018.
- [24] S. Shin, D. Alyasiri, M. D'Auria, W. J. Otter, C. W. Myant, D. Stokes, Z. Tian, N. M. Ridler, and S. Lucyszyn, "Fully 3-D printed tunable microwave subsystem," in *Proc. IEEE MTT-S Int. Microw. Workshop Ser. Adv. Mater. Process. (IMWS-AMP)*, Bochum, Germany, Jul. 2019, pp. 43–45.
- [25] I. Robertson and S. Lucyszyn, "Phase shifters," in *RFIC and MMIC Design and Technology*, Hertfordshire, U.K.: The Institution of Engineering and Technology, 2009, pp. 381–427.
- [26] S. Koul and B. Bhat, "Mechanical phase shifters," in *Microwave and Millimeter Wave Phase Shifters*, vol. 1. Boston, MA, USA: Artech House, 1991, pp. 72–73.
- [27] W. L. Stutzman and G. A. Thiele, *Antenna Theory and Design*. Hoboken, NJ, USA: Wiley, 2013, pp. 294–405.
- [28] J. F. Aurand, "Pyramidal horns. I. Simple expressions for directivity as a function of aperture phase error," in *Dig. Antennas Propag. Soc. Int. Symp.*, San Jose, CA, USA, vol. 3, Jun. 1989, pp. 1435–1438.
- [29] Cura. (2018). *Ultimaker*. Accessed: Nov. 10, 2018. [Online]. Available: <https://ultimaker.com/en/products/ultimaker-cura-software>
- [30] G. F. Engen and C. A. Hoer, "Thru-reflect-line: An improved technique for calibrating the dual six-port automatic network analyzer," *IEEE Trans. Microw. Theory Techn.*, vol. 27, no. 12, pp. 987–993, Dec. 1979.
- [31] A. Rumiantsev and N. Ridler, "VNA calibration," *IEEE Microw. Mag.*, vol. 9, no. 3, pp. 86–99, Jun. 2008.
- [32] N. M. Ridler, "News in RF impedance measurement," in *Proc. 27th Gen. Assem. Int. Union Radio Sci. (URSI)*, Maastricht, The Netherlands, Aug. 2002, pp. 1–4, Paper 374.
- [33] N. M. Ridler, "A review of existing national measurement standards for RF and microwave impedance parameters in the UK," in *Proc. IEEE Colloquium Microw. Meas., Current Techn. Trends*, Feb. 1999, pp. 6–1–6–6.
- [34] Z. Tian, S. F. Gregson, and D. G. Gentle, "Recent advances in antenna pattern measurement at millimetre wave frequencies in a spherical near-field range," in *Proc. Loughborough Antennas Propag. Conf.*, Nov. 2018, p. 5.
- [35] *IEEE Standard Test Procedures for Antennas*, IEEE Standard 149-1979, 1979.
- [36] A. C. Newell, R. C. Baird, and P. F. Wacker, "Accurate measurement of antenna gain and polarization at reduced distances by an extrapolation technique," *IEEE Trans. Antennas Propag.*, vol. 21, no. 4, pp. 418–431, Jul. 1973.
- [37] C. R. Garcia, R. C. Rumpf, H. H. Tsang, and J. H. Barton, "Effects of extreme surface roughness on 3D printed horn antenna," *Electron. Lett.*, vol. 49, no. 12, pp. 734–736, Jun. 2013.



SANG-HEE SHIN (S'19) was born in Seoul, South Korea, in 1992. He received the M.Eng. degree in aeronautical engineering from Imperial College London, London, U.K., in 2018.

After graduation, he joined the Electrical and Electronic Engineering Department as a Ph.D. Student. His research interest includes designing and 3-D printing RF devices for microwave applications.



DIYAR F. ALYASIRI was born in Baghdad, Iraq, in 1995. He received the M.Eng. degree in electrical and electronic engineering from Imperial College London, London, U.K., in 2017, where he focused on applying additive manufacturing techniques in the design of low-cost RF devices.

He undertook an industrial placement with BAML as a Technology Analyst, with a focus on functional programming for accelerated parallel processing.



MARIO D'AURIA received the M.Sc. degree in electronic engineering from the Second University of Naples, in 2010, and the Ph.D. degree from Imperial College London, in 2015. His research interests include LTCC, silicon laser micromachining, and 3-D printing for RF and microwave applications.



ZHENG RONG TIAN received the M.Sc. degree in electromagnetic theory and microwave techniques from the Beijing Institute of Technology, Beijing, China, in 1994, and the Ph.D. degree in microwave communications from Middlesex University, Middlesex, U.K. in 2002.

She is currently a Higher Research Scientist with the National Physical Laboratory, Middlesex. She is responsible for NPL's spherical near field antenna test range.



WILLIAM J. OTTER received the M.Eng. degree in electrical and electronic engineering and the Ph.D. degree from Imperial College London, London, U.K., in 2010 and 2015, respectively.

During his M.Eng. degree, he undertook industrial placements with the BAE Systems Advanced Technology Centre, Great Baddow, U.K., and held an IET FUSE scholarship. Throughout his Ph.D., he held the Val O'Donoghue Scholarship with the Department of Electrical and Electronic Engineering.

He was a Postdoctoral Research Associate with Imperial College London, working in the area of millimeter-wave and THz bio-sensors. His research interests include 3-D printing, photonic crystals, low-cost terahertz devices, electromagnetic modeling, optoelectronics, and electromagnetic sensors.



NICK M. RIDLER (M'03–SM'06–F'14) received the B.Sc. degree from King's College London, University of London, London, U.K., in 1981.

He is currently the Head of Science in the Electromagnetic and Electrochemical Technologies Department, National Physical Laboratory, U.K. He is also a Visiting Professor with the universities of Leeds, Liverpool, and Surrey, U.K., and the Non-Executive Director of LA Techniques Ltd. He is the Past President of ARFTG (the Automatic RF Techniques Group).

He has more than 35 years' experience working in industrial, government, and academic research establishments. His main research interest includes precision high-frequency electromagnetic measurement (from 1 kHz to 1 THz).

Mr. Ridler is a fellow of the Institution of Engineering and Technology (IET) and a fellow of the Institute of Physics (IOP). He was the Chair of the IEEE MTT Society's Standards Coordinating Committee. He is the Chair of the IEEE P1785 Standard Working Group for Waveguides for Millimeter and Sub-Millimeter Wavelengths. He represents the IEC (International Electrotechnical Commission) on the International Bureau of Weights and Measures (BIPM) Joint Committee for Guides in Metrology (JCGM) Working Group 1 Expression of Uncertainty in Measurement (GUM).



CONNOR W. MYANT received the bachelor's degree in mechanical engineering from the University of Exeter, in 2006, and the Ph.D. degree from Imperial College London, in 2010, on the development of experimental techniques for investigating lubricated, compliant, and bearing contacts.

He was with the ICL Tribology Group, where he held a Junior Research Fellowship, studying synovial fluid lubrication of artificial articular joints. He is currently a Lecturer with the Dyson School

of Design Engineering, Imperial College London, and a Co-Lead for the Imperial College Additive Manufacturing Network. He is also a Module Lead for solid mechanics 2 and design for additive manufacture.



STEPAN LUCYSZYN (M'91–SM'04–F'14) received the Ph.D. degree in electronic engineering from King's College London, University of London, London, U.K., in 1992, and the D.Sc. degree (Hons.) in millimeter-wave and terahertz electronics from Imperial College London, London, in 2010.

From 1997 to 2012, he taught MMIC measurement techniques on IEE/IET short courses hosted by the National Physical Laboratory, U.K. He is currently a Professor of millimetre-wave systems and the Director of the Centre for Terahertz Science and Engineering, Imperial College London. He has coauthored over 200 papers and 12 book chapters in applied physics and electronic engineering.

Prof. Lucyszyn was a fellow of the Institution of Electrical Engineers, U.K., and the Institute of Physics, U.K., in 2005. He was a Founding Member of the Steering Group for the U.K.'s EPSRC Terahertz Network and a member of the IEEE Technical Committee for Terahertz Technology and Applications (MTT-4). In 2008, he became a fellow of the Electromagnetics Academy, USA. He was appointed as an IEEE Distinguished Microwave Lecturer, from 2010 to 2013. He is currently a European Microwave Lecturer for the European Microwave Association. He co-founded the Imperial College London spin-out company Drayson Wireless Ltd., in 2014.



DANIEL STOKES received the MPhys degree in physics with astrophysics from the University of Kent, in 2012.

He is currently a Higher Research Scientist with the Electromagnetic Measurements Group, National Physical Laboratory (NPL), Teddington, U.K., with a focus on S-parameter and power traceability in guided wave mediums.

...